Experimental and Numerical Investigations of the Role of Proppant Embedment on Fracture Conductivity in Narrow Fractures

Ming Fan and **Zihao Li,** Virginia Tech; **Yanhui Han,** Aramco Services Company: Aramco Research Center–Houston; and **Yuntian Teng** and **Cheng Chen,** Virginia Tech

Summary

With the advancement of drilling and completion technologies in unconventional reservoirs, more extended reach wells are developed, and narrow-fracture environments are created in these reservoirs. Proppant embedment in monolayer/thin-layer-propped fractures can be significantly different from multilayer-propped fractures. In this study, a comprehensive investigation combining laboratory experiments with numerical simulations was conducted to explore the factors affecting proppant embedment and induced fracture conductivity loss in narrow fractures. The fracture-conductivity experiments were performed using monolayers of sand and ceramic proppant particles sandwiched between Berea Sandstone and Eagle Ford Shale plates under different closure pressures. The experiment study demonstrated that the long-term rock/fluid interaction leads to significant proppant embedment, and the fracture having a rough rock surface has higher fracture conductivity in monolayer-propped fractures. To further quantify the influence of proppant layer number, size, distribution variations, and particle crushing on proppant embedment, a numerical modeling approach that coupled continuum mechanics, discrete element method (DEM), and the lattice Boltzmann (LB) method was developed. In the simulation, the fracture/proppant system was constructed by filling proppant, modeled by DEM, between two fracture surfaces that were modeled by FLAC3D (Itasca Consulting Group 2012); LB simulation was then performed on the changing proppant pack to compute its time-dependent permeability. The numerical model was validated by comparing numerical results with measured fracture conductivities in the laboratory experiment. The simulation results demonstrated a strong correlation between proppant embedment and rock mechanical properties. When the Young's modulus of the rock plate is less than 5 GPa, large magnitudes of proppant embedment can be expected in fractures supported by monolayers of ceramic proppant particles. Moreover, large-size proppant particles are more sensitive to the variations of Young's modulus of the rock plate. When the rock formation in a narrow fracture environment has a relatively high Young's modulus, the proppant diameter distribution has a lesser effect on the fracture conductivity. The outcome of this study will provide insights into the role of reservoir rock characteristics, proppant properties, and closure pressure on proppant embedment in narrow fractures.

Introduction

Hydraulic fracturing (HF) is widely used to enhance hydrocarbon extraction from challenging unconventional reservoirs because of their low permeability and complex petrophysical properties (Zhang et al. 2017; Li et al. 2019). With the advancement in shale drilling and completions, more extended reach wells and complex fracture networks are developed, which vastly improves recovery rates and economical payback from unconventional reservoirs (Gu et al. 2017; Bandara et al. 2019; Li et al. 2020). During the completion stage of the well development, proppant slurries are injected into hydraulically created fractures to keep them open and to maintain conductive channels between the reservoir and wellbore once the high HF pressure is released (Liang et al. 2016). In the near-wellbore fracture networks where fracture aperture is wide, a higher concentration of 2 or 4 lb/ft^2 of proppant particles are often injected into fractures to provide a sufficient conductivity for hydrocarbon production. At such a high proppant concentration, proppant embedment has little impact on the evolution of the fracture conductivity (Fan et al. 2019b). As the fracture network grows into far regions away from the wellbore, the fracture width gets smaller, and a more complex fracture network system is created in unconventional reservoirs. In a narrow fracture environment, the realistic proppant injection concentration can be 0.25 to 0.5 lb/ft^2 or less (Fuss et al. 2016; Herskovits et al. 2017). In an extreme case, a monolayer of microproppant particles may be injected with fracturing fluids into preexisting natural fractures or newly created microfractures (Liang et al. 2020). Proppant embedment in these monolayer/thin-layer-propped fracture networks can deteriorate the fracture conductivity significantly, if not completely, which poses new challenges on the proppant selection and placement designs.

Proppant embedment has been identified as damage to the fracture conductivity in unconventional hydrocarbon reservoirs for many years (Stegent et al. 2010; Cui et al. 2014). Despite that proppant embedment in wide fractures filled with proppant packs have been extensively investigated (Fan et al. 2017b), few studies have focused on proppant embedment in narrow fractures. The proppant embedment-induced fracture conductivity loss in narrow fractures could differ significantly from those fractures filled with multilayer proppant packs. When the proppant concentration is low, some proppant particles can be completely embedded into the rock formation under high closure pressures, proppant particles then lose the capability to support the fracture, and eventually the fracture aperture and conductivity may suffer significant reductions. Therefore, it is of critical importance to identify proppant embedment mechanisms in narrow fractures. In the study of Khanna et al. (2012), a semianalytical solution was proposed to estimate the conductivity in narrow fractures filled with monolayers of proppant particles. However, this model ignores the effects of proppant properties, such as proppant type, proppant size, and proppant distribution, thus failing to accurately delineate the fracture conductivity evolution in response to increasing closure pressures. Darin and Huitt (1960) also developed a semiempirical correlation to estimate the proppant embedment depth in thin-layer-propped fracture networks, but the influence of reservoir rock properties on proppant embedment is not considered. These studies indicate that it is imperative to take both reservoir rock characteristics and proppant properties into consideration in terms of the assessment of proppant embedment in narrow fractures.

Original SPE manuscript received for review 13 April 2020. Revised manuscript received for review 6 July 2020. Paper (SPE 204222) peer approved 31 August 2020.

During hydrocarbon production, reservoir pressure depletes, effective stress of the rock matrix increases, and subsequently more loads are transferred to proppant particles; as a result, proppant particles penetrate into the rock formation and proppant embedment occurs (Fan et al. 2017a). The role of rock properties on the interactions between a rock formation and proppant has been explored in many studies. Alramahi and Sundberg (2012) studied the effect of shale mineral composition and mechanical properties on proppant embedment in a fracture filled with a monolayer of proppant particles. Their studies revealed that a low Young's modulus of shale could lead to significant proppant embedment and fracture conductivity reduction. According to Jansen et al. (2015), the Young's modulus as well as the fracture surface roughness of a rock formation control the fracture conductivity of a monolayer-propped fracture, which is also consistent with the experiment result of Perez Pena et al. (2016). Singh et al. (2019) conducted proppant embedment tests on unconventional shale rocks that were exposed to different fracturing fluids and reported that using fresh water alone as the fracturing fluid could lead to significant proppant embedment and corresponding reduction in the fracture conductivity. Zhong et al. (2019) further studied the shale softening effect on proppant embedment with time by soaking shale samples in brine solutions for a period of 2 hours and 10 days. The experiment results show that shale rocks with high clay contents are more susceptible to the alteration of rock mechanical properties and have greater proppant embedment depths. Therefore, proppant embedment mechanisms in narrow fracture networks, which are complicated by the variations of rock characteristics in terms of their response to different closure pressures, require more thorough and comprehensive studies.

In addition to the reservoir rock characteristics, proppant properties such as proppant size, type, distribution, and concentration/proppant layer number are also vital to determine the severity of damage to the conductivity due to proppant embedment in narrow fractures. Chen et al. (2015) combined X-ray computerized-tomography imaging with LB simulation to study the interaction between the rock matrix and proppant for fractures supported by monolayers of proppant particles. The results demonstrate that proppant embedment of a fracture filled with a monolayer of proppant particles is more sensitive to the effective stress compared with a fracture filled with multiple layers of proppant particles. Zhang et al. (2015) performed a numerical analysis using computational fluid dynamics to study the impact of the number of layers on proppant embedment and observed severe proppant embedment in monolayer-propped fractures. Tang et al. (2018) also investigated the influence of proppant layer number on proppant embedment through both experimental and numerical studies. They reported that a proppant coverage of 150% on the fracture face (i.e., 1.5 layers of proppant) is the optimal proppant concentration to reduce proppant embedment. Nevertheless, none of these studies has investigated all the important proppant characteristics when assessing the role of proppant embedment on the conductivity in narrow fractures. In recent years, it has been a common practice in industry to use small mesh-size proppants, such as 30/50 or 40/70 with slickwater fracturing fluids for fracture treatments in unconventional reservoirs because they can easily be transported into deeper regions of fracture networks (Bandara et al. 2019; Fan et al. 2020). Moreover, it remains unclear as to how small mesh-size proppants affect proppant embedment and conductivity in fractures filled with low concentrations of proppants. Both laboratory studies, numerical simulations, and industry practice indicate that the assessment of the effect of varying proppant characteristics on proppant embedment is critical to efficient proppant placement and effective reservoir conductivity in narrow fractures.

In this work, we strive to study the factors affecting proppant embedment in narrow fractures including fracture-closure pressure, reservoir rock and proppant properties, and rock/fluid interaction through both experimental and numerical approaches. We first conducted fracture conductivity experiments to study the influences of rock/fluid interaction, fracture surface roughness, and proppant type on proppant embedment. In the next step, the factors affecting proppant embedment in narrow fractures, including proppant layer number, size, distribution, and particle crushing, were investigated through numerical simulations. In the numerical modeling approach, the coupling of continuum mechanics code and DEM code was employed to simulate proppant embedment, compaction, rearrangement, and crushing. The discretized pore structure of the proppant pack was then used as interior boundary conditions of flow modeling in the LB simulation of fluid flow through the pore space. Through the simulation, the proppant embedment behavior in narrow fractures can be examined under increasing closure pressures in conjunction with the variations in Young's modulus of the reservoir rock. The outcome of this study will benefit the optimization of HF operations through probing the interactions between the rock formation and proppant particles in narrow-fracture environments.

Overview of the Study of Proppant Embedment in Narrow Fractures

This work combined both laboratory experiments and numerical simulations to study the proppant embedment behavior in narrow fractures. In this study, a narrow fracture indicates that the proppant has a monolayer structure or small layer number (i.e., up to three layers of proppant) in the fracture space. We first conducted fracture conductivity measurements to evaluate the conductivity loss due to the rock/fluid interaction. Both mesh-20/40 sand and ceramic proppant particles were placed uniformly with a full monolayer proppant concentration between two Berea Sandstone plates, which were soaked in deionized (DI) water for a period of 2 hours and 21 days before the conductivity tests, respectively. Next, to study the influence of fracture surface roughness on proppant embedment, a monolayer of mesh-20/40 ceramic proppant particles were placed uniformly between Eagle Ford Shale plates having rough and smooth fracture surfaces. Because it is difficult to quantify the influences of proppant layer number, proppant size, proppant distribution, and proppant crushing on proppant embedment in laboratory experiments, these effects were evaluated through numerical simulations. To validate the numerical model, we first conducted fracture conductivity experiments for ceramic proppant at the concentrations of 2 lb/ft^2 using steel plates. The microscopic properties of ceramic proppant in the model were calibrated by comparing the fracture conductivity-closure pressure curve monitored in the simulation with that recorded in the laboratory experiment. In the second set of simulations, the rock plate mechanical properties were calibrated by comparing the simulation results with laboratory data of sandstone plates immersed in DI water for 2 hours and 21 days as well as Eagle Ford Shale plates having smooth surfaces using ceramic proppant. In the third set of simulations, with the calibrated mechanical parameters of the sandstone rock plates, the sand's microscopic property and crushing strength were calibrated through comparing the simulations results with laboratory data of sandstone plates soaked in DI water for 2 hours and 21 days. **Fig. 1a** illustrates the calibration workflow for sand and ceramic proppant's microscopic properties as well as rock plate mechanical properties. Equipped with the calibrated sand, ceramic proppant, and rock plate mechanical parameters, numerical simulations were designed to unravel the roles of proppant layer number, size, distribution, particle crushing on proppant embedment, and the fracture conductivity evolution in narrow fractures.

In the numerical study, the rock plate was modeled using Mohr-Coulomb-type solid elements provided by FLAC3D, and the proppant pack was simulated by the particle assemblage generated using Particle Flow Code 3D (PFC3D; Itasca Consulting Group 2008) directly. The proppant embedment-induced mechanical interactions between the rock plates, and proppant particles under different closure pressures were simulated through FLAC3D/PFC3D coupling. The fracture closure due to proppant compaction, rearrangement, and crushing under increasing mechanical loading (induced by reservoir depletion) was simulated using PFC3D. The gradual increase of the closure pressure was realized by applying a constant velocity on the top rock plate to drive the rock/proppant interactions. To achieve a balance between computational accuracy and efficiency, different loading velocities were tested; a velocity of 10^{-9} m/step, with which the system seemed to

give a quasistatic response, was chosen for the simulations in this work. The fracture was then closing in the *z*-direction (the direction normal to fracture face) at a constant velocity, which was adequately slow to avoid rapid surge of effective stress between proppant particles and to allow the fluid within the pore space to flow away in the lateral (*x*-*y*) directions. In this manner, the rock/proppant system was in a quasisteady state; that is, the transient effects of pore pressure and resultant stress changes on proppant particles were negligible (Fan et al. 2018b). An in-house numerical code was developed to discretize the pore structure of the proppant pack at a resolution of 0.02 mm/pixel, and the discretized pore structure was then imported into the LB simulator as interior boundary conditions of fluid flow modeling to measure the fracture permeability. The integrated simulation workflow for modeling proppant compaction, rearrangement, embedment, and particle crushing, as well as the influence on fracture conductivity, is illustrated in Fig. 1b. Using this numerical simulation, we are able to study various factors that affect the change of fracture conductivity induced by proppant embedment, rearrangement, compaction, and particle crushing through directly modeling the interactions between the rock formation and proppant particles. The combination of experimental and numerical studies provides insights into the factors affecting conductivity loss induced by proppant embedment in narrow fractures, which has the potential to benefit optimization processes for proppant placement, completion design, and well production.

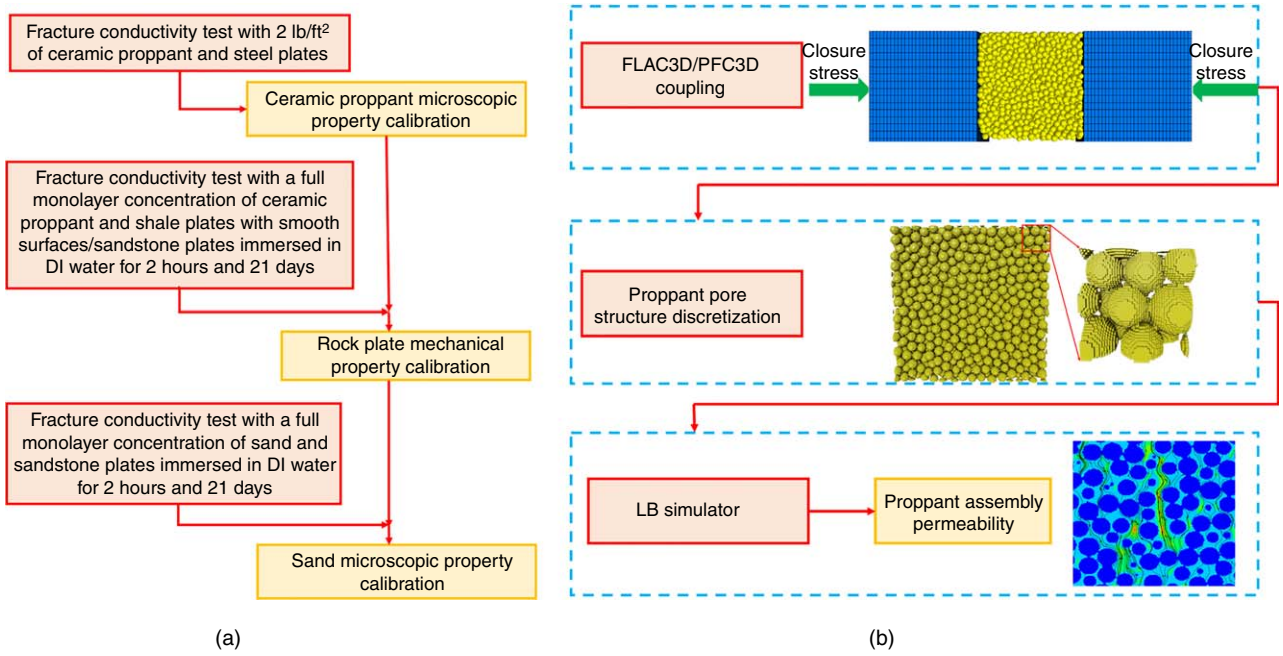

(a) (b)

Fig. 1—(a) Calibration workflow of sand and ceramic proppant's microscopic properties as well as rock plate mechanical properties; and (b) integrated simulation workflow for modeling proppant compaction, rearrangement, embedment, and particle crushing, as well as the influence on fracture conductivity.

Methods

Experiment Description. The Berea Sandstone and Eagle Ford Shale plates were prepared according to the API standard for conductivity cells (*API RP-19D* 2008) with a dimension of 7 in. in length, 1.5 in. in width, and 0.5 in. in thickness. In one pair of Eagle Ford Shale plates, fractures were carefully induced along the laminated bedding plane to create rough fracture surfaces. For the Berea Sandstone used in this study, kaolinite comprised a large fraction of the clay minerals, which accounted for 10% of the total mineralogy. Other clay minerals (montmorillonite, illite, etc.) were also identified but were present only in trace amounts. DI water was injected into the fracture with a rate of 0.1 cm^3/min at room temperature (20°C). During the process of HF, the fracturing fluid infiltrates the fracture interacts with the rock formation and causes softening of the reservoir rocks. To evaluate the conductivity loss due to the rock/fluid interaction in HF treatments, the Berea Sandstone plates were soaked in DI water for a period of 2 hours and 21 days before the conductivity tests, respectively. During the fracture conductivity measurement test, the closure pressure was gradually increased to 41.4 MPa (6,000 psi), and the fracture conductivities under different closure pressures were recorded. We first tested the conductivity for 20/40-mesh ceramic proppant with a concentration of 2 lb/ft^2 using steel plates to calibrate ceramic proppant's microscopic parameters for the PFC3D model. Next, the fracture conductivity experiments were performed using Berea Sandstone plates having smooth surfaces. The mesh-20/40 sand and ceramic proppant particles were placed uniformly with a full monolayer proppant concentration between the two sandstone plates. The rock plate mechanical properties were extracted by comparing numerical results with laboratory-measured fracture conductivity data. The proppants in the fracture conductivity measurement cell using Berea Sandstone plates are illustrated in **Fig. 2.** It can be clearly observed that ceramic proppant particles have a much higher sphericity and roundness than sand particles, which increases the porosity and permeability of the proppant pack. To study the influence of fracture surface roughness on proppant embedment, monolayers of mesh-20/40 ceramic proppant particles were placed between Eagle Ford Shale plates having smooth and rough rock surfaces, respectively. During the fracture conductivity experiment, the fracture width is determined by the difference of top- and bottom-plate displacements recorded directly by the displacement transducer. The fracture conductivity defined by *API RP-19D* (2008) is given by:

$$kw_f = \frac{100 \cdot \mu \cdot Q \cdot L}{w \cdot \Delta p}, \qquad (1)$$

where kw_f is the conductivity of the fracture ($\mu\text{m}^2 \cdot \text{cm}$); μ is the viscosity of fracturing fluids (mPa·s); Q is the flow rate (cm^3/s); L is the distance between pressure ports (cm); w is the width of the conductivity cell (cm); and $\Delta p (p_{\text{upstream}} - p_{\text{downstream}})$ is the pressure drop (kPa). The monitored flow rate and pressure drop were then imported into Eq. 1 to determine the fracture conductivity at each closure pressure. Each experiment was repeated twice, and similar results were observed.

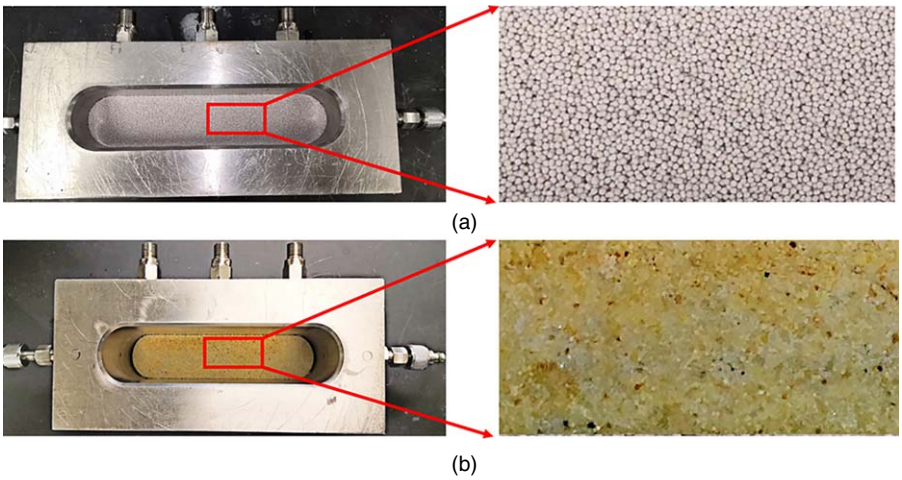

Fig. 2—(a) Ceramic proppant, and (b) sand proppant in the fracture conductivity measurement cell.

The particle size distributions of mesh-20/40 sand and ceramic proppant used in fracture conductivity experiments are illustrated in **Fig. 3.** For ceramic proppant, the majority of particles falls between mesh-20 and mesh-30; for sand, particle diameters are more evenly distributed in the entire range of mesh-20/40. Compared to ceramic proppant, sand particles have a more heterogeneous particle-diameter distribution in a proppant pack, where smaller particles move more easily and can be compressed into the pore space between larger particles, leading to a more significant proppant compaction and rearrangement. The large fracture-closure distance in a fracture supported by sand results in a high porosity, permeability, and fracture conductivity reduction (Fan et al. 2018b).

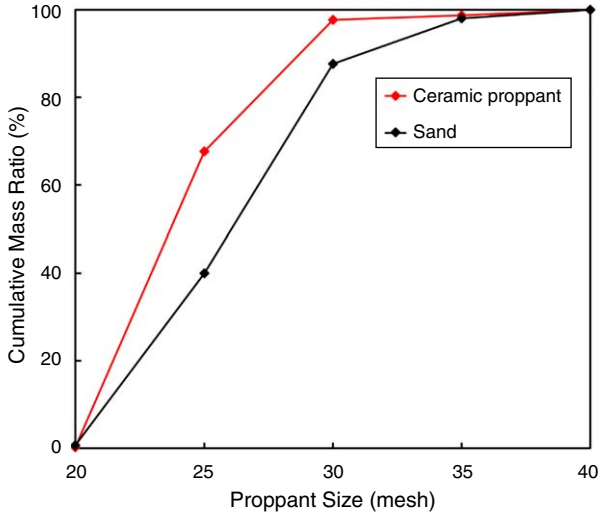

Fig. 3—Particle-size distributions for the mesh-20/40 sand and ceramic proppant. The *y*-axis indicates the cumulative mass fraction of the particles that are larger than a specific particle size marked on the *x*-axis.

Continuum Mechanics and FLAC3D. Continuum mechanics software FLAC3D is used for numerical simulation of rock plates in this work. FLAC3D is an explicit finite-difference program for modeling 3D mechanical behaviors of elastoplastic geomaterials and their interactions with fluid flow, heat transfer, and structural elements in both static and dynamic analysis modes (Itasca Consulting Group 2012). It offers dozens of built-in elastic, elastoplastic, and rheological constitutive models for modeling different geomaterials under various loading conditions. In FLAC3D, a computational loop solves two sets of governing equations: the constitutive law at elements and the equations of motion at grid points. A general FLAC3D solution procedure includes modeling geometry of geomaterials with zones, assignment of constitutive models and material properties, applications of boundary and initial conditions, execution of the simulation, and post-processing of modeling results.

DEM and PFC3D. In this study, a 3D discontinuum mechanics simulator, PFC3D, was used for DEM simulations (Itasca Consulting Group 2008). DEM was initiated by Cundall (1971) then extended by Cundall and Strack (1979) to study rock mechanics and soil problems using an assembly of rigid, spherical particles. Recently, DEM has been proven efficient in simulating the mechanical behaviors of proppant particles (Fan et al. 2019a, 2019b; Zhu et al. 2019). In PFC3D, the spherical particles are generated independently and interact only at contacts or interfaces. The calculation cycle adopts a time-stepping algorithm, in which the position and velocity of each particle is determined by Newton's second law of motion, and the force/displacement relation is used to update the contact force at each contact. During the simulation, contacts can be created and separated. However, Newton's second law of motion is not applied to boundary walls because the motion of walls is specified by the user (Itasca Consulting Group 2008). In the proppant compaction study, only the frictional grain behaviors need to be modeled. The microscopic properties for the model include the modulus E_a, the ratio of

normal to shear stiffness at particle contacts k_n/k_s, and the coefficient of friction u. The relationship between apparent modulus and particle stiffness is defined by:

$$k_n = AE_a/D, \quad \ldots\ldots (2)$$

where $A = \pi r^2$, $r = \begin{cases} \min(\mathrm{R}^1, \mathrm{R}^2), & \text{ball-ball} \\ \mathrm{R}^1, & \text{ball-wall} \end{cases}$, $D = \begin{cases} \mathrm{R}^1 + \mathrm{R}^2, & \text{ball-ball} \\ \mathrm{R}^1, & \text{ball-wall} \end{cases}$, R^1 and R^2 are the radii of the two particles in contact.

Coupling FLAC3D with PFC3D. In the coupling model, the continuum mechanics model is built with FLAC3D, and the DEM model is built with PFC3D. During the coupling process, FLAC3D cycles and sends the interface zone velocities to the top and bottom faces in the PFC3D model. These velocities act as the loading force on the proppant pack in the PFC3D model, and the calculated contact forces on the top and bottom faces of the proppant pack are sent back to the interface zones in the FLAC3D model. This back and forth sending and receiving velocities and contact forces continues until the equilibrium is reached. The coupling interface adopts a Socket I/O connection technique for data exchange (Itasca Consulting Group 2008; Fan et al. 2018a; Wang et al. 2020).

Proppant Crushing Model. In the particle-crushing model, when a particle is overloaded by contact forces, the particle is crushed and its volume in the assembly is replaced by a cluster of smaller particles. In DEM, the stress tensor within a particle can be obtained from the volumetric average of contact forces acting on the particle (Potyondy and Cundall 2004):

$$\sigma_{ij} = \frac{R}{V}\sum_{c=1}^{n_c} n_i^{(c)} F_j^{(c)}, \quad \ldots\ldots (3)$$

where R is the radius of the particle, V is the volume of the particle, n_c is the number of contacts, $n_i^{(c)}$ is the ith component of the unit direction vector of contact c, and $F_j^{(c)}$ is the jth component of the force magnitude of contact c.

The characteristic particle stress σ_s is used as the criterion of octahedral shear stress to determine particle crushing (Wang et al. 2020):

$$\sigma_s = \frac{1}{3}\left[(\sigma_1 - \sigma_2)^2 + (\sigma_2 - \sigma_3)^2 + (\sigma_1 - \sigma_3)^2\right]^{1/2}, \quad \ldots\ldots (4)$$

where σ_1, σ_2, σ_3 are the three principal stresses.

When the characteristic stress surpasses the particle crushing strength, the particle breaks and the particle breaking criterion is determined by Eq. 5:

$$\sigma_s > \sigma_{\mathrm{crush}}. \quad \ldots\ldots (5)$$

In this work, the fragmentation of a particle is simulated by replacing the particle with four smaller particles, and the replaced particles can also break during subsequent simulation process, as illustrated in **Fig. 4.** The replaced particles have two radii with values of 0.5 R and 0.33 R. To conserve the original particle volume, the four small particles are then increased by a factor of 1.4559 (Zheng and Tannant 2019). In this study, the sand particle is assumed spherical, and the generated smaller particles inherit the same microscopic properties from the big particle.

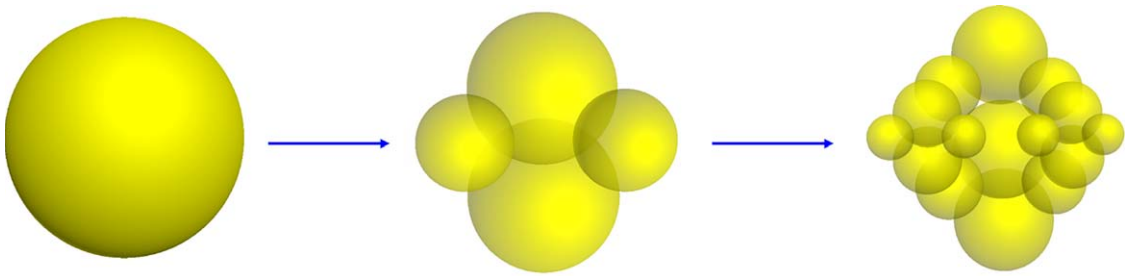

Fig. 4—Particle-crushing process: a big particle is replaced by several small particles after crushing.

Discretization of 3D Proppant Pore Structure. The 3D proppant pore structure from the DEM simulation was discretized, extracted, and then imported into the LB model as interior boundary conditions of flow modeling in the simulation of single-phase Darcy flow through the pore space. Specifically, the 3D pore geometry was discretized with a 3D mesh grid having a resolution of 0.02 mm per LB length unit in the x-, y-, and z-directions.

LB Method. The LB method is a mesoscopic physics-based numerical method for recovering the Navier-Stokes equations through solving a set of kinetic equations at the mesoscale (Chen and Doolen 1998; Succi 2001). The LB simulator used in this study has been extensively verified and validated by direct comparisons with analytical solutions and laboratory measurements (Chen et al. 2008, 2009a, 2009b). It was then optimized with high-performance graphics processing unit through parallel computing, which enhanced the computational speed by a factor of 1,000 and led to an in-house LB code, graphics processing unit-enhanced LB simulator (Chen et al. 2016). In this work, the D3Q19 (19 velocity vectors in 3D space) lattice structure was used because of its advantage in achieving a good balance between computational stability and efficiency (Chen et al. 2013).

Particle distribution in the Bhatnagar-Gross-Krook-based, single-relaxation-time LB equation is given by

$$f_i(\mathbf{x}+\mathbf{e}_i\Delta t, t+\Delta t) = f_i(\mathbf{x}, t) - \frac{f_i(\mathbf{x}, t) - f_i^{\mathrm{eq}}(\rho, u)}{\tau} \quad (i = 0, 1, 2 \ldots 18), \quad (6)$$

where $f_i(\mathbf{x}, t)$ is the particle-distribution function specifying the probability that fluid particles at lattice location $\mathbf{x}$ and time t travel along the ith direction; $\boldsymbol{e}_i$ is the lattice velocity vector; Δt is the timestep; τ is the dimensionless relaxation time; ρ is the macroscopic fluid density; $\mathbf{u}$ is the macroscopic fluid velocity; and $f_i^{\mathrm{eq}}(\rho, \mathbf{u})$ is the equilibrium distribution function selected to recover the macroscopic Navier-Stokes equations.

For fluid flow simulation in the Darcy regime, we imposed a periodic boundary condition with a constant pressure difference in the longitudinal direction and no-slip boundary conditions on the four lateral sides and interior solid surfaces (Inamuro et al. 1999; Chen et al. 2009a). Because proppant particle packing is isotropic, permeabilities measured in the x- and y-directions (i.e., the two principal directions parallel to the top and bottom fracture walls) are nearly identical. The Re number was much smaller than one to ensure that the macroscopic flow was well within the Darcy regime. At the continuum scale, the Darcy velocity $\mathbf{v}$ is calculated by averaging the pore-scale flow velocity of each lattice node in the pore space throughout the entire computational domain. One can calculate the permeability tensor using the Darcy's law:

$$\mathbf{v} = -\frac{1}{\mu}\mathbf{k} \cdot \nabla p, \quad (7)$$

where $\mathbf{v} = \left[v_x, v_y, v_z\right]^T$ is the Darcy velocity; $\mathbf{k} = k_{ij}(i, j = x, y, z)$ is the permeability tensor, with i being the flow direction and j being the pressure gradient direction; ∇p is the pressure gradient; and μ is the dynamic viscosity of the fluid. More details about the LB simulator and the associated graphics processing unit optimization can be found in our previous papers (Chen et al. 2016; Fan et al. 2018b; Fan and Chen 2020). In this study, the fracture wall is assumed impermeable, and thus no mass flux is allowed in the direction perpendicular to the fracture wall.

Numerical Model Setup. In the coupled FLAC3D-PFC3D model, rock plates are simulated with Mohr-Coulomb material in FLAC3D based on the continuum-scale mechanics. The width, length, and height of the rock block were 10, 10, and 5 mm, respectively. The rock block was divided into a 30 × 30 × 15 mesh, which can achieve a balance between computational workload and accuracy. The proppant particles filling the fracture between rock plates were modeled by PFC3D based on the discrete-scale mechanics. The dimension in the x-y plane, which was parallel to the fracture face, was 10 × 10 mm, whereas the initial height of the proppant pack (i.e., fracture width) depended on the proppant concentration and proppant size. Proppant concentration is defined as the mass of proppant particles per unit fracture-face area and usually in the unit of lb/ft^2. The proppant particles were generated randomly with well-controlled diameter distributions and wrapped by six walls. The top and bottom walls in the PFC3D model were in direct contact with rock plates modeled by FLAC3D, whereas the four side walls in the PFC3D model were used to prevent particles from escaping out of the fracture. In each calculation loop, the velocities at the top and bottom surfaces of the fracture in the FLAC3D model were monitored and sent to the PFC3D model. In the meanwhile, the reaction forces on the proppant particles in direct contact with the rock plates in the PFC3D model were recorded and then sent to the FLAC3D model. Consequently, the stress boundary conditions for the FLAC3D model and the velocity boundary conditions in the PFC3D model were updated. The data communication between the FLAC3D model and PFC3D model continued until a specified closure pressure was reached. The coupling scheme and data transfer workflow in the FLA3D/PFC3D coupled numerical model is illustrated in **Fig. 5.**

Fig. 5—FLAC3D/PFC3D-coupled numerical model.

Proppant Embedment Determination. In this study, the displacements of grid points on rock plate surfaces in contact with proppant particles after proppant embedment simulations are characterized quantitatively by surface displacement parameters. The most commonly used parameter is the average displacement, which is the arithmetic average of the absolute values of surface profile height deviations from the mean line. Nevertheless, due to the wide range of proppant diameters, the average displacement may fail to provide enough evaluation of local surface displacements. To obtain more proppant embedment details, the peaks and valleys on the rock plate surface displacement profile can be evaluated separately (Santos and Júlio 2013). Therefore, the surface displacement of rock plate after proppant embedment tests can be characterized by the mean peak height R_p, mean valley depth R_v, and mean peak-to-valley height R_a. **Fig. 6** illustrates peaks and valleys on a sample surface displacement profile over a scale of equally divided five blocks.

The mean peak height is defined by

$$R_p \approx \frac{1}{m}\sum_{i=1}^{m}|p_i|. \quad (8)$$

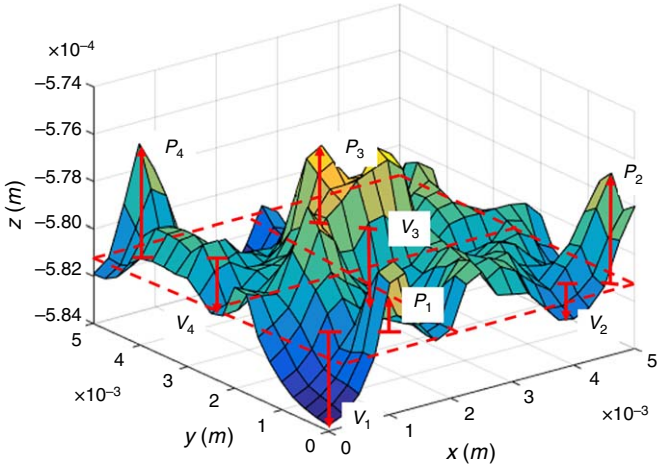

Fig. 6—Illustration of surface displacement profile over a spatial scale of four equal-sized blocks.

The mean valley depth is given by

$$R_v \approx \frac{1}{m}\sum_{i=1}^{m}|V_i|. \quad \ldots\ldots (9)$$

The mean peak-to-valley height is defined as the average of mean valley depth and peak height, which is given by

$$R_a = \frac{1}{2}(R_v + R_P), \quad \ldots\ldots (10)$$

where P_i is the maximum peak height in the ith block, V_i is the maximum valley depth in ith block, and m is the number of the divided blocks from the sample surface. In this study, R_a is adopted to evaluate the proppant embedment depth and the rock plate surface is divided into nine equal-sized blocks.

Results

Effect of Rock/Fluid Interaction. To investigate the fracture conductivity evolution because of the rock/fluid interaction induced rock softening in HF treatments, Berea Sandstone plates were soaked in DI water for 2 hours and 21 days separately and then used in the conductivity measurements with both ceramic and sand proppant particles. The proppant particles were placed uniformly between rock plates at a full monolayer proppant concentration. The fracture conductivity experiments conducted using the rock plates soaked in DI water for 2 hours demonstrated that ceramic proppant withstood a higher closure pressure, whereas sand proppant was crushed into finer grains after the conductivity experiments, as illustrated in **Figs. 7a and 7c**. This was because the higher roundness of the ceramic proppant helped improve its crushing resistance, whereas the irregular shape of the sand proppant increased the probability of crushing and fragmentation during the experiments (Nakata et al. 2001; Karatza et al. 2019). The conductivity experiments using the rock plates soaked in DI water for 21 days showed that the rock plate in direct contact with ceramic proppant was indented significantly because the rock plates were softened after 21 days of rock/fluid interactions, as shown in Fig. 7b. In addition, sand crushing was alleviated because of the softened rock surface induced by the rock-fluid interactions, as shown in Fig. 7d.

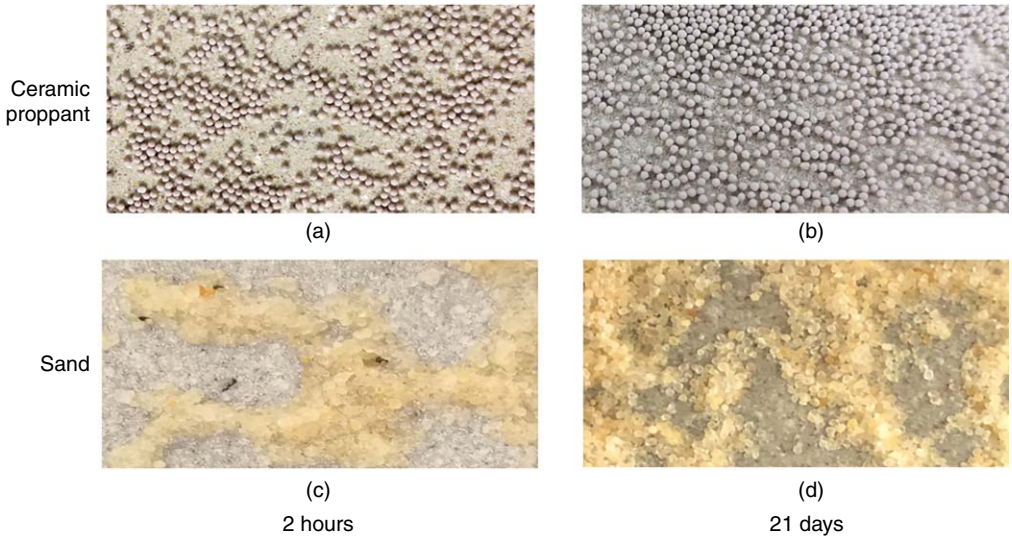

Fig. 7—Proppant particles on sandstone rock surfaces after fracture conductivity measurements under closure pressures. Specifically, two pairs of sandstone rock plates were soaked in DI water for (a) 2 hours and (b) 21 days separately before the conductivity measurements using ceramic proppant, and another two pairs of sandstone rock plates were soaked in DI water for (c) 2 hours and (d) 21 days separately before the conductivity measurements using sand proppant.

Fig. 8a illustrates the fracture width as a function of closure pressure for fractures supported by different types of proppants. Because crushed sand grains were flushed to the downstream of the conductivity cell, the fluid outlet was blocked by crushed fines, leading to the failure of conductivity measurement at 41.4 MPa. The fracture widths for fractures supported by sand declined much faster compared to fractures supported by ceramic proppant. At a lower closure pressure (6.9 MPa), the fracture width reductions for both sand and ceramic proppant can be attributed to proppant embedment. Because sand has poor sphericity and roundness, the irregular shape of sand may help increase the fracture width in a monolayer-propped fracture when the longer dimension of a sand particle is perpendicular to the fracture face. When the fracture is subjected to a relatively higher closure pressure, more sand particles are crushed into finer grains, resulting in a rapid decline of fracture width. Moreover, larger particles have a lower crushing resistance than smaller particles (Zheng et al. 2018), leading to an increased crushing ratio of sand and thereby large fracture width reduction. The comparison of the experiment results of 2 hours with 21 days clearly demonstrates that the rock/fluid interaction softens the rock plate and increases the proppant embedment depth.

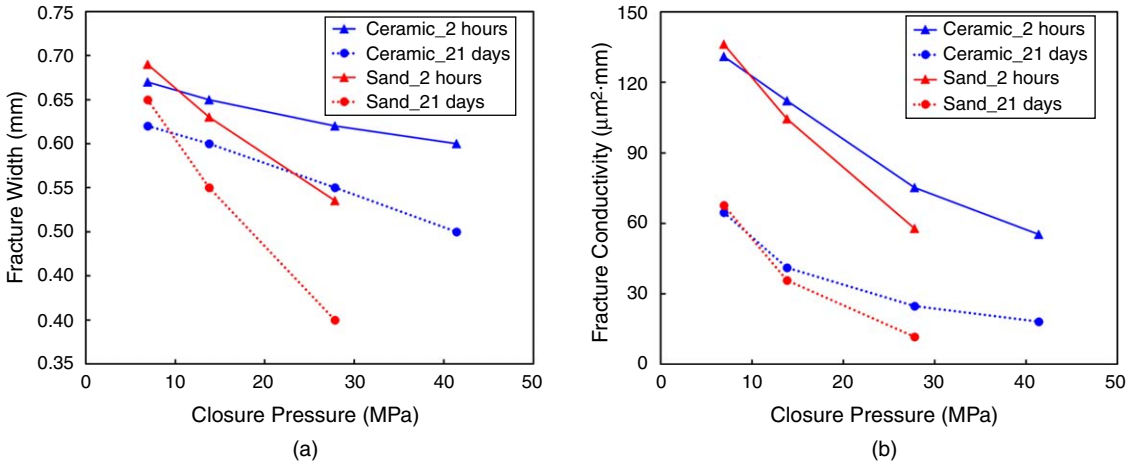

Fig. 8—(a) Fracture width and (b) fracture conductivity as a function of closure pressure in the fracture conductivity experiments using Berea Sandstone plates.

Fig. 8b presents the fracture conductivity as a function of closure pressure for fractures filled with sand and ceramic proppant particles. At the closure pressure of 6.9 MPa, fractures supported by sand had slightly higher fracture conductivities than fractures supported by ceramic proppant because of larger fracture widths and enhanced flow channels. As the closure pressure increases, more sand particles are crushed into finer grains, which leads to a fast decline in the fracture conductivity. It is also worth noting that, as illustrated in Fig. 7d, fewer sand particles were crushed between rock plates that were immersed in DI water for 21 days, which helped mitigate the fracture conductivity reduction. Compared to experiments using rock plates upon exposure to DI water for 2 hours, the small fracture conductivity of experiments using rock plates immersed in DI water for 21 days was because the conductivity loss resulting from proppant embedment surpassed the conductivity gain due to less fine grain generation. The experiment results indicate that the short-term rock/fluid interaction will not lead to severe proppant embedment, whereas the long-term rock-fluid interaction can cause substantial proppant embedment and damage to the fracture conductivity. When narrow fractures are subjected to higher closure pressures, sand crushing can deteriorate the fracture conductivity significantly even for situations where proppant embedment is alleviated in softer reservoir formations due to the rock/fluid interaction.

Effect of Fracture Surface Roughness. To investigate the fracture surface roughness on proppant embedment, fracture conductivity experiments were conducted using monolayers of mesh-20/40 ceramic proppant particles and Eagle Ford Shale plates having both smooth and rough rock surfaces, as illustrated in **Figs. 9a and 9b**. Compared to the plate with smooth surface, it is impossible to place a monolayer of proppant particles uniformly over the plate having a rough rock surface, as shown in Figs. 9c and 9d. Because of the surface asperities, proppant particles are more likely to accumulate at surface valleys, whereas proppant particles fail to collect at surface hills.

Fig. 9—Eagle Ford Shale plates having (a) smooth rock surface and (b) rough rock surface, and proppant placements on the plates having (c) smooth rock surface and (d) rough rock surface in the fracture conductivity cell.

Fig. 10a illustrates the fracture width as a function of closure pressure for shale plates having smooth and rough rock surfaces at a monolayer proppant concentration. At the same closure pressure, the shale plate having a rough surface had a higher fracture width. Compared to the smooth surface, proppant particles on the rough surface tend to have more than one contact point with the rock plate, which helps to distribute the closure pressure and to mitigate proppant embedment. Fig. 10b illustrates the fracture conductivity as a function of closure pressure for fractures formed with smooth and rough rock surfaces. It is clearly observed that experiments using Eagle Ford Shale plates having rough fracture surfaces had higher fracture conductivities. Because of the spherical shape of ceramic proppant, there are more open spaces at the location adjacent to the fracture surface than the fracture center in the monolayer-propped smooth fracture. Proppant embedment in smooth fractures will reduce both the fracture width and permeability significantly, leading to a smaller fracture conductivity. However, in the monolayer-propped rough surface fracture, the uneven fracture surface helps to create more void space in the middle of the fracture because the body centers of proppant particles are not necessarily lined up due to fracture surface asperities. This will create more large flow channels and preferential flow paths and, consequently, the fractures with rough surfaces have higher permeabilities and fracture conductivities.

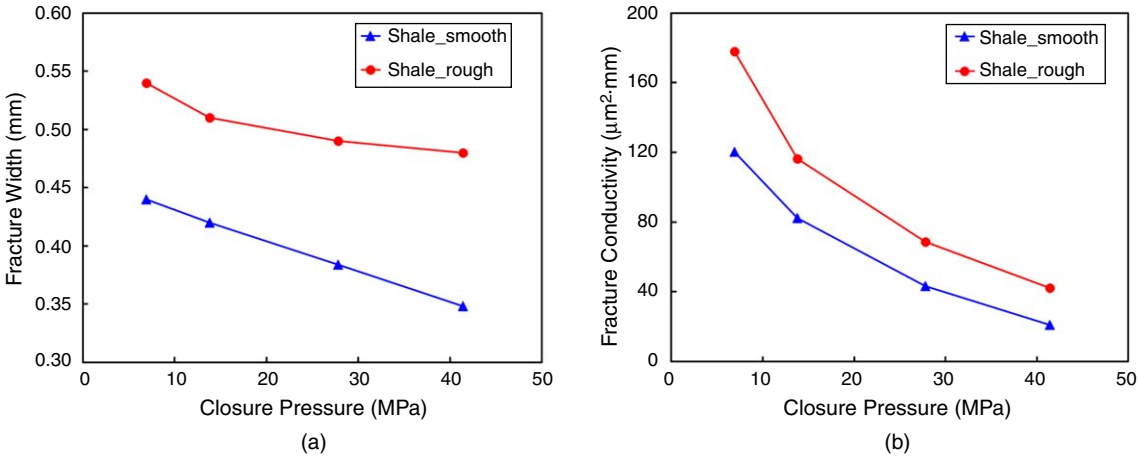

Fig. 10—(a) Fracture width and (b) fracture conductivity as a function of closure pressure in the fracture conductivity experiments using Eagle Ford Shale plates.

Numerical Model Verification and Parameter Calibration. The first set of simulations were designed to reproduce the fracture conductivity experiments for ceramic proppant with a concentration of 2 lb/ft^2. Because the fracture conductivity was tested using steel plates, there was no proppant embedment, and the fracture closure was due to proppant compaction and rearrangement. The model was constructed with mesh-20/40 particles having a ceramic proppant diameter distribution illustrated in Fig. 3. **Fig. 11** illustrates that the fracture conductivities predicted by numerical simulations have a good agreement with experimental results, and the fracture conductivity decreases with increasing closure pressure. The microscopic properties of ceramic proppants in the model were calibrated through comparing the fracture conductivity-closure pressure curve monitored in the simulation with that recorded in the laboratory experiment. The microscopic properties of ceramic proppant extracted from simulations are summarized in **Table 1.**

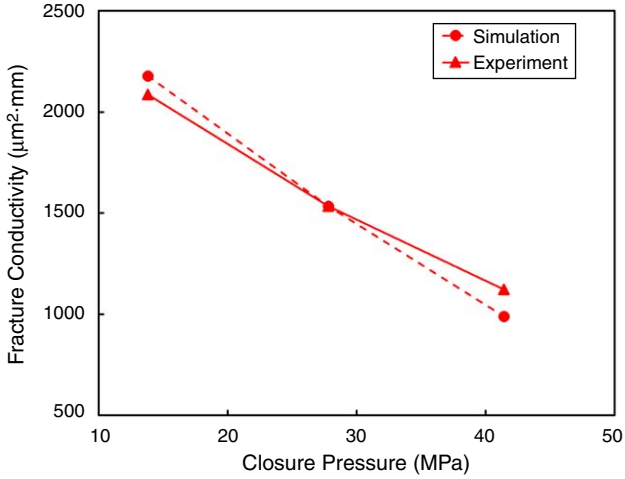

Fig. 11—Comparison between numerical results and experiment measurements. The ceramic proppant conductivities were tested with a proppant concentration of 2 lb/ft^2 using steel plates.

Proppant Type	Proppant Diameter (mm)	Bulk Modulus (GPa)	Stiffness Ratio k_n/k_s	Coefficient of Friction u	Density (kg/m^3)
Ceramic	0.42 to 0.84	0.35	1	0.5	2650

Table 1—Microscopic properties of ceramic proppant used in the PFC3D model.

In the second set of simulations, the mechanical properties of rock plate were calibrated by comparing the simulation results with laboratory data of sandstone plates immersed in DI water for 2 hours and 21 days as well as Eagle Ford Shale plates having smooth surfaces. As illustrated in **Fig. 12,** the numerical model was further verified by the good agreement between simulation results and experimental data in a different set of conductivity tests. Note the microscopic properties of ceramic proppant calibrated from the first set of simulations were adopted in this set of simulations. We performed a parametric study of rock mechanical properties by isolating the effect of each individual property of the rock plate. The parameter calibration results indicate that the effect of Poisson's ratio on the fracture conductivity is slight, which is also consistent with the analytical study from Guo and Liu (2012). The rock plate experienced somewhat tensile and compressive failure, but the plastic parameters (i.e., tensile strength, cohesion, friction angle) seem to only have little effect on the fracture conductivity. In other words, the embedment here is primarily elastic local deformation in the rock plate; for example, after the closure pressure is unloaded, the residual depth of embedment cavities on the rock plate becomes relatively trivial. It is observed that the proppant embedment depth is affected significantly by the changes in Young's modulus of the rock plate. The calibrated mechanical parameters of shale plates with smooth surfaces as well as sandstone rock plates after 2 hours and 21 days of DI water soaking are listed in **Table 2.** The calibration of rock mechanical parameters indicates that the rock/fluid interaction decreases the Young's modulus of the reservoir rock, leading to large proppant embedment depth and fracture conductivity loss.

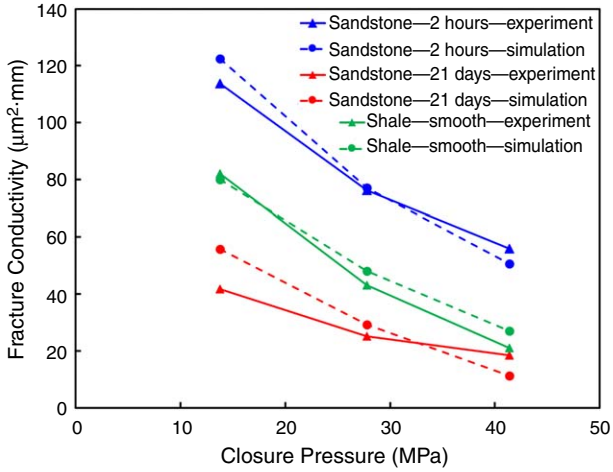

Fig. 12—Fracture conductivity as a function of closure pressure obtained from laboratory fracture conductivity experiments and numerical simulations with shale/sandstone plates and a monolayer of ceramic proppant. The time frame of 2 hours and 21 days indicates that rock plates were soaked in DI water for a period of 2 hours and 21 days before conductivity tests, respectively. Shale smooth indicates the shale rock plates have smooth surfaces.

Property	Sandstone—2 Hours	Sandstone—21 Days	Shale—Smooth
Young's modulus, E (Pa)	20×10^9	1×10^9	2×10^9
Poisson's ratio (ν)	0.25	0.25	0.25
Cohesive strength, C (Pa)	30×10^6	30×10^6	30×10^6
Friction angle, φ (°)	30	30	30
Tensile strength, σ^T (Pa)	25×10^6	25×10^6	25×10^6

Table 2—Mechanical properties of rock plates in the FLAC3D model.

In the third set of numerical simulations, the sand's microscopic properties and crushing strength were calibrated by comparing the simulation results with laboratory data of sandstone plates soaked in DI water for 2 hours and 21 days. The model was built with a monolayer of mesh-20/40 sand particles using the sand particle-diameter distribution shown in Fig. 3. The sandstone plate's mechanical properties were adopted from Table 2. **Fig. 13** presents good agreements between numerical simulations and experimental results. Through matching the fracture conductivity-closure pressure curves measured from experiments with those recorded in numerical simulations, the sand's microscopic properties and crushing strength threshold were calibrated and summarized in **Table 3.**

Effect of Proppant Layer Number. During unconventional hydrocarbon production, narrow-fracture environments supported by monolayers or thin layers of proppant particles are more easily generated because of the increasing fracture length. In this section, fractures filled with one to three layers of ceramic proppant particles were modeled to investigate the influence of proppant layer number on proppant embedment and fracture conductivity. The particles followed the mesh-20/40 ceramic proppant diameter distribution illustrated in Fig. 3. **Fig. 14** displays side views of fractures supported by proppant packs with one to three layers. All the models were constructed with the calibrated mechanical properties of proppant and rock plates listed in Tables 1 and 2.

Fig. 15 illustrates a visual representation of proppant embedment into rock plates at different closure pressures (13.8, 27.8, and 41.4 MPa) and Young's moduli (0.5, 1, and 5 GPa). It was clearly observed that the proppant embedment depth increased with the increase of the closure pressure and decreased with the increase of the rock plate Young's modulus. Moreover, when the Young's modulus of the rock plate exceeded 5 GPa, only minor indentation on the surface of rock plate was observed. Fig. 15 indicates that the proppant embedment depth is strongly correlated with the Young's modulus change in the reservoir rock.

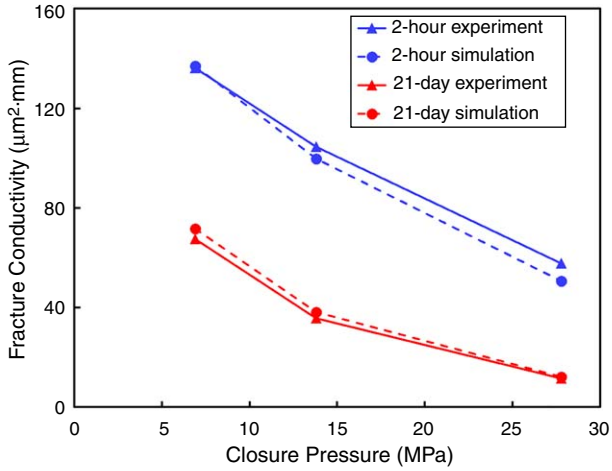

Fig. 13—Comparison between numerical results and experiment measurements. A monolayer of sand particles was placed between sandstone plates that were soaked in DI water for 2 hours and 21 days separately before the conductivity measurements.

Proppant Type	Proppant Diameter (mm)	Bulk Modulus (GPa)	Crushing Strength (MPa)	Stiffness Ratio (k_n/k_s)	Coefficient of Friction (u)	Density (kg/m^3)
Sand	0.42 to 0.84	0.2	50	1	0.5	1540

Table 3—Microscopic properties of sand used in the PFC3D model.

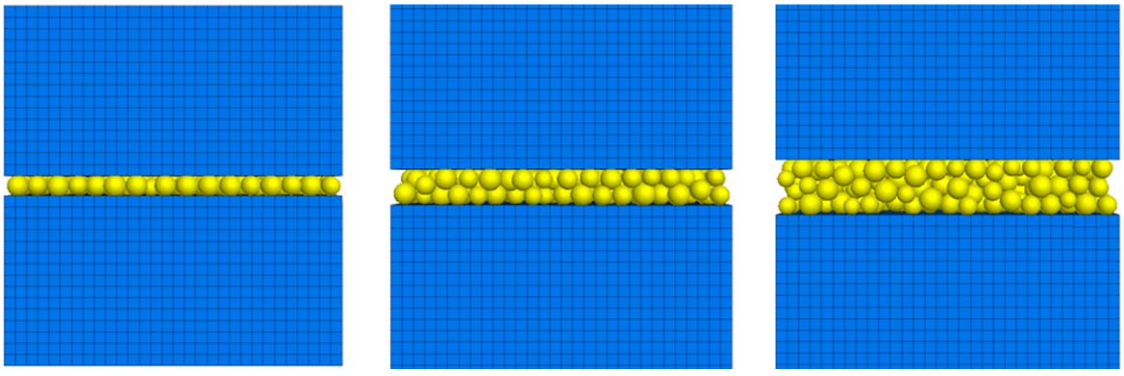

Fig. 14—Side views of fractures supported by (a) monolayer, (b) two layers, and (c) three layers of ceramic proppant.

When the fracture surface is covered by a monolayer of proppant particles, proppant embedment into the rock surface is the only factor affecting the fracture closure (note, for the given closure pressure in the test, no ceramic proppant was crushed). If proppant particles develop to a multilayer assembly, all the mechanisms including proppant compaction, rearrangement, and embedment will contribute to the fracture closure. Therefore, when the fracture is filled with a monolayer of proppant particles, the proppant embedment depth is equal to the fracture width reduction. When the fracture is supported by a multilayer proppant assembly, the proppant embedment depth is determined by the fracture width reduction difference between the rock plate with real Young's modulus and the rock plate with high Young's modulus (no proppant embedment). In this study, only proppant embedment of the top rock plate surface is determined due to the complementary surface configuration of the top and bottom rock plates.

Fig. 16 presents the proppant embedment depth as a function of rock plate Young's modulus under different closure pressures when fractures are supported by monolayer, two-layer, and three-layer numbers of proppant particles. As expected, the proppant embedment depth increased with the increase of the closure pressure and decreased with increasing Young's modulus of the rock plate. When the Young's modulus of the rock plate exceeded 5 GPa, proppant embedment depths for fractures filled with different layer numbers of proppant particles gradually reached stable values. It is also observed that when the proppant layer number increased, the proppant embedment depth decreased. This was because when proppant particles developed to multilayers, due to the proppant compaction and rearrangement, the number of particles in direct contact with fracture walls was increasing, which led to less load on individual particles to resist, eventually decreasing the proppant embedment depth.

Fig. 17a illustrates the fracture closure as a function of rock plate Young's modulus for fractures supported by different layer numbers of proppant particles. The fracture width is determined by the difference of top and bottom plates' mean peak-to-valley heights using Eq. 7. Fracture width reduction is defined as the ratio of the amount of fracture width decrease to the original fracture width. It can be observed that fracture closure decreased with increasing proppant layer numbers because fractures can be supported by more proppant particles, allowing a single particle to undertake less load. Fig. 17b demonstrates fracture conductivities for fractures filled with proppant particles from monolayer to multilayers under different closure pressures. The simulation results demonstrated that

fracture conductivity increased with the number of proppant layers. When the Young's modulus of the rock plate is 0.5 GPa, proppant embedment can reduce the fracture aperture by 60%, and it is difficult to maintain sufficient conductivity for the fracture supported by a monolayer of proppant particles. Due to the spherical shape of ceramic proppant, large flow channels are formed adjacent to the fracture surface than the fracture center when a fracture is filled with a monolayer of proppant particles. Proppant embedment will lead to a significant decrease in the fracture permeability and an ultimate loss in the fracture conductivity. When proppant particles develop to a multilayer structure, the permeability reduction because of proppant embedment can be mitigated because large flow channels can be formed within the proppant pack. Therefore, mechanical support from two- or three-layer numbers of proppant particles are able to impede the fracture width reduction, increase the fracture permeability, and thereby maintain the conductivity for a narrow fracture.

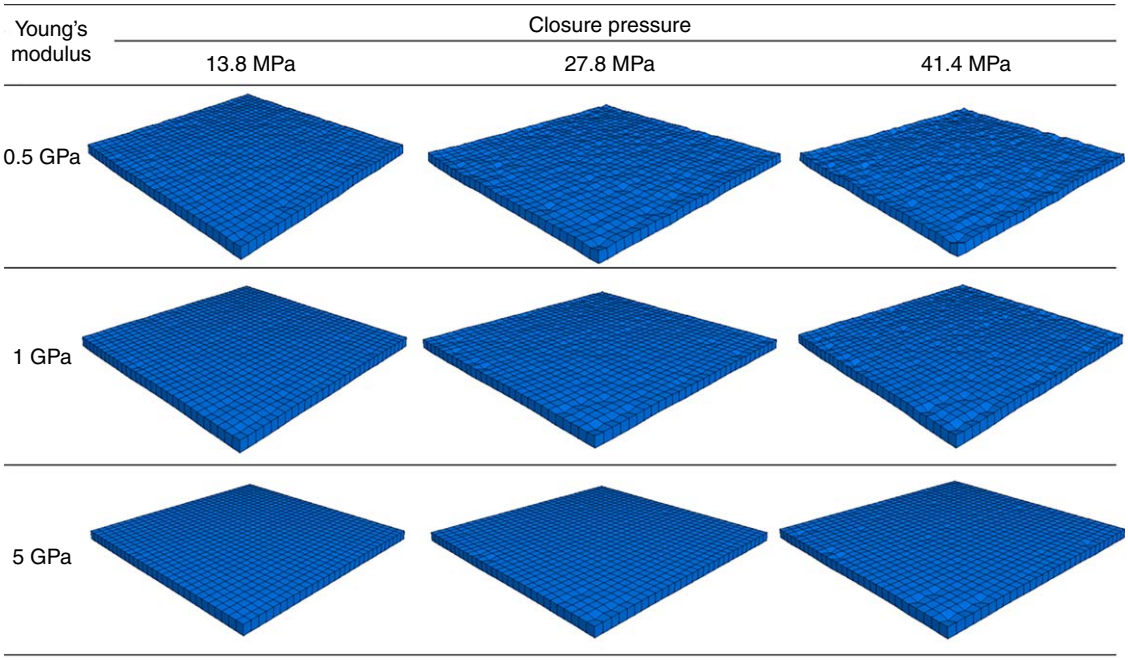

Fig. 15—Rock plate surface indented by a monolayer of proppant particles with different rock plates' Young's moduli and closure pressures.

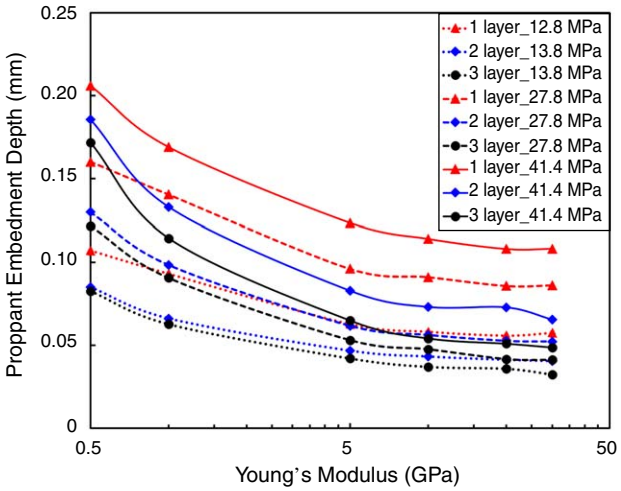

Fig. 16—Proppant embedment depth as a function of rock plate Young's modulus under different closure pressures and proppant layer numbers.

Effect of Proppant Size. **Fig. 18** presents the effective stress distributions on the rock plate surface in direct contact with proppant particles under different closure pressures. The narrow fractures were supported by proppant packs with mesh-40/70 and mesh-20/40 proppants at a full monolayer proppant concentration. Both mesh-20/40 and mesh-40/70 particles followed the ceramic proppant diameter distribution illustrated in Fig. 3. The color intensity is proportional to the magnitude of the effective stress. The fracture surface in contact with mesh-40/70 proppant particles had a more uniform stress distribution. In comparison to mesh-20/40 proppant particles, mesh-40/70 proppant particles have a much smaller diameter so the fracture can be supported by more proppant particles, which reduces the effective mechanical load on each particle and embedment depth on the rock surface. At the closure pressure of 41.4 MPa, large indentations of mesh-20/40 particles can impose high local stress on the reservoir rock surface, which may generate fine particles that will be produced within the formation fluids.

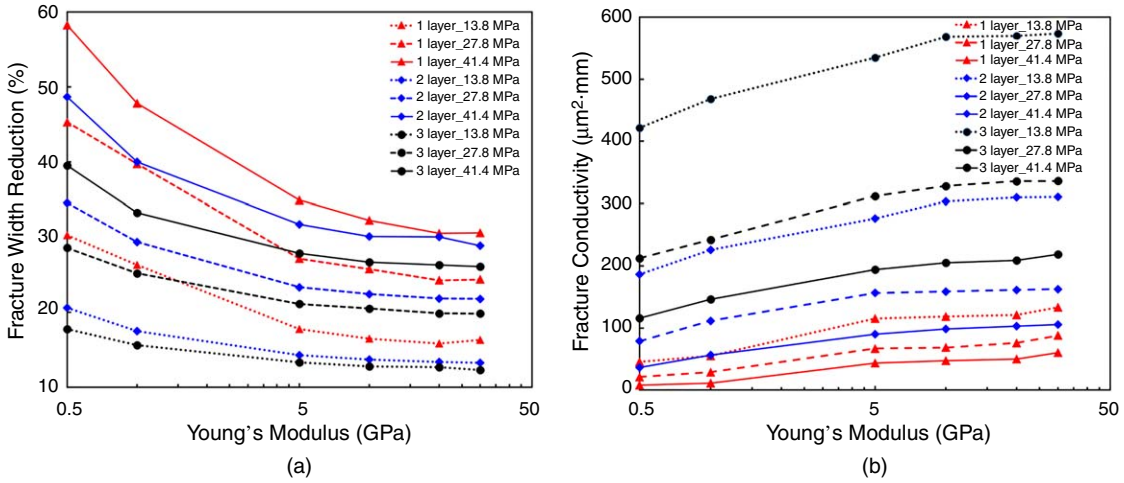

Fig. 17—(a) Fracture width reduction and (b) fracture conductivity as a function of rock plate Young's modulus for fractures filled with monolayer, two layers, and three layers of proppant particles under different closure pressures.

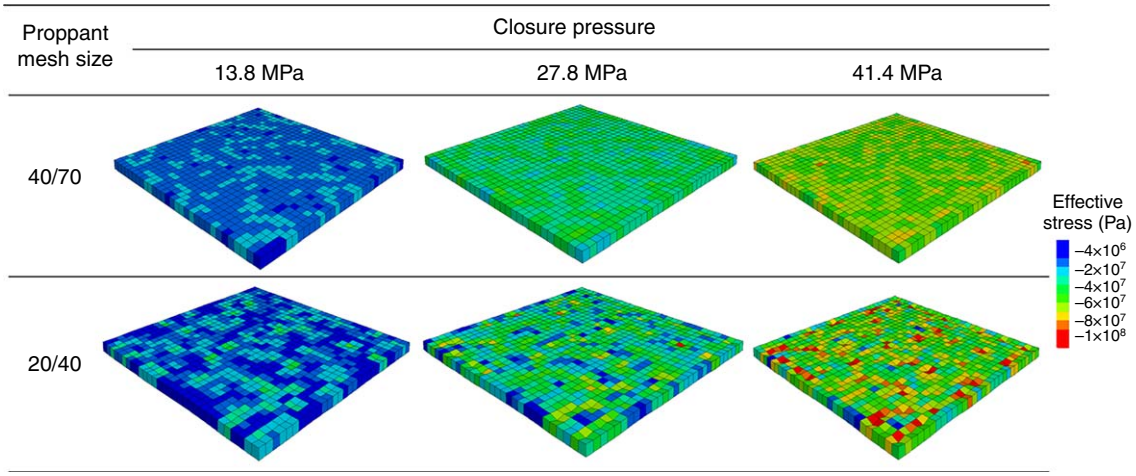

Fig. 18—Effective stress distributions on rock surfaces indented by mesh-40/70 and mesh-20/40 proppants under different closure pressures. The fractures are filled with monolayer proppant packs with a rock Young's modulus of 1 GPa.

Fig. 19a illustrates the fracture width reduction as a function of rock plate Young's modulus for fractures supported by three mesh-size proppant packs. As expected, proppant embedment decreased with increasing Young's modulus of the rock plate. The embedment with mesh-20/40 was more noticeable than mesh-40/70 and mesh-100 proppants. Moreover, the fracture width reduction ratio (embedment ratio) decreased when the mesh size of proppant decreased. This was because, when the fine-sized proppant was used, more particles were in direct contact with the rock surface and thus played an effective role in supporting the fracture, which reduced the load on individual particles. As a consequence, the rock plate was less susceptible to proppant embedment. Fig. 19b presents the fracture conductivity as a function of rock plate Young's modulus. It can be observed that fractures filled with large-size proppant particles had higher fracture conductivities compared with fractures filled with small-size proppant particles. In the fractures supported by mesh-20/40 proppant particles, as more large flow channels can be formed in the proppant pack, the fracture conductivity gain from permeability increase will surpass the fracture conductivity loss introduced by proppant embedment (i.e., aperture reduction). In the fractures filled with mesh-40/70 and mesh-100 proppant particles, both the reduction in permeability of the proppant pack and the reduction of fracture width will work together, resulting in a smaller fracture conductivity. Moreover, the fracture conductivity as a function of Young's modulus curves demonstrate that large-size proppant particles are more sensitive to the changes in Young's modulus of the rock plate. In narrow fractures filled with small mesh-size proppant particles, the long-term fracture conductivity can be maintained more easily because more void spaces on the rock surface can be covered by proppant particles.

Effect of Proppant Diameter Distribution. **Fig. 20** presents effective stress distributions for rock plate surfaces in direct contact with proppant particles with homogeneous and heterogeneous particle-diameter distributions under different closure pressures. In the first panel, fractures are supported by monolayers of homogeneous proppant particles with a particle diameter equal to 0.63 mm. In the second panel, fractures are supported by monolayers of mesh-20/40 particles with the ceramic proppant diameter distribution illustrated in Fig. 3. It is clearly illustrated that fracture surfaces in contact with homogeneous proppant particles had a more homogeneous stress distribution. This was because in the fractures supported by heterogeneous proppants, not all the particles were in direct contact with both the top and bottom fracture surfaces, leading to a more heterogeneous stress distribution.

Fig. 21a illustrates the fracture width reduction as a function of rock plate Young's modulus for fractures filled with monolayers of proppant particles having different diameter distributions. When rock plates had the same Young's modulus, fractures supported by homogeneous proppant particles had a smaller fracture width reduction. This was because all the proppant particles were in contact with both top and bottom fracture surfaces, leading to a lower load on an individual proppant particle and thereby smaller proppant

embedment. Fig. 21b presents the fracture conductivity as a function of rock plate Young's modulus. In general, the fracture supported by homogeneous proppant particles had a higher fracture conductivity because of the higher fracture width and permeability. However, when the rock plate Young's modulus was 0.5 GPa, the fracture filled with heterogeneous proppant particles had a relatively higher fracture conductivity under effective stress of 41.4 MPa. This was because the large proppant embedment led to more reductions in flow channels and subsequent conductivity loss in the monolayer proppant pack having a homogeneous proppant diameter distribution. It is also interesting to note that, when the rock plate Young's modulus was 30 GPa, fractures filled with heterogeneous proppant particles had relatively higher facture conductivities. This was because the proppant assembly with a heterogeneous particle distribution had more large-size proppant particles that could lead to more open flow channels and thus a higher fracture conductivity when proppant embedment was less severe. This study indicates that when the reservoir rock has a relatively high Young's modulus, the proppant particle-diameter distribution has a lesser effect on the fracture conductivity.

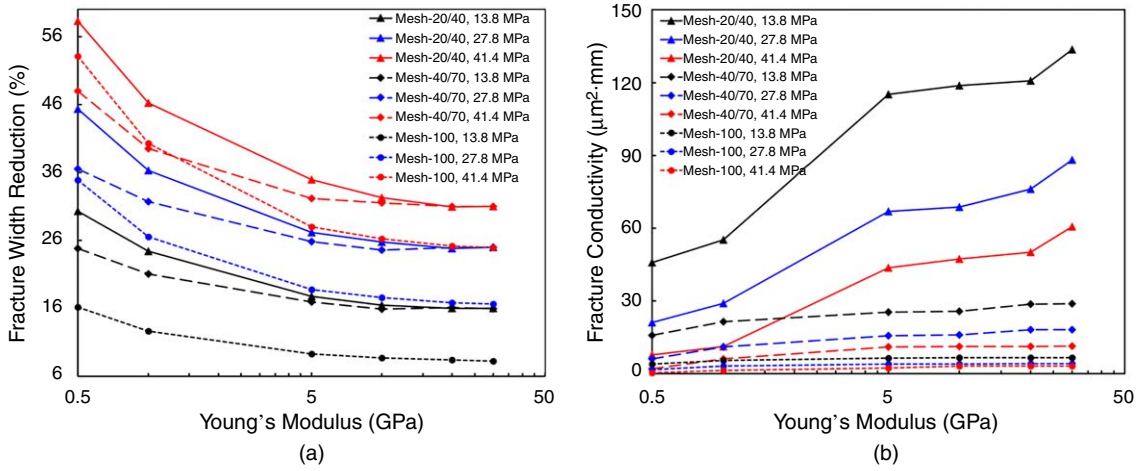

Fig. 19—(a) Fracture width reduction and (b) fracture conductivity as a function of rock plate Young's modulus for fractures supported by monolayer proppant packs having various proppant sizes.

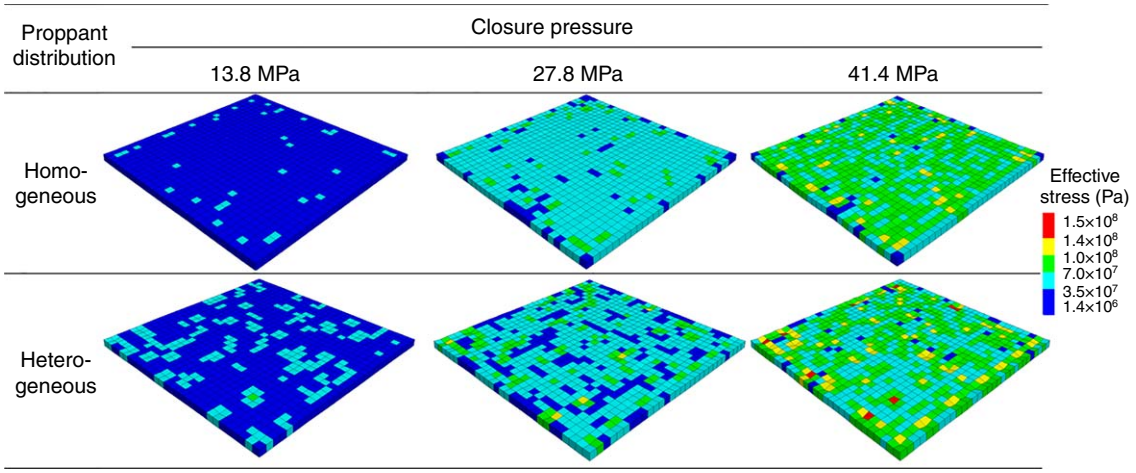

Fig. 20—Effective stress distributions on rock surfaces indented by monolayers of proppants with homogeneous and heterogeneous particle-diameter distributions under different closure pressures. The Young's modulus of the rock plate is 1 GPa.

Effect of Proppant Crushing. After fracture conductivity experiments, it was observed that sand was crushed into finer grains under high closure pressures. In this section, fractures filled with sand proppant packs having different layer numbers, particle sizes, and size distributions were simulated to investigate the effect of proppant crushing on proppant embedment and fracture conductivity. The mesh-40/70 and mesh-20/40 proppant particles followed the sand particle-diameter distribution, as shown in Fig. 3. **Fig. 22** illustrates the fractures filled with monolayers of sand particles under different closure pressures. The numerical model was based on the calibrated properties listed in Tables 2 and 3. It was clearly illustrated that, when the closure pressure increased to 4,000 psi, several particles failed to withstand the closure pressure and began to break. When the fracture was subjected to a closure pressure of 6,000 psi, most particles were crushed into fine grains, and the mechanical loading imposed on the fine particles in direct contact with fracture surfaces further increased, which enhanced proppant embedment on rock surfaces.

Fig. 23a illustrates the proppant embedment ratio as a function of closure pressure. Proppant embedment ratio is defined as the ratio of proppant embedment depth to the original fracture width. As expected, with the same closure pressure, the proppant embedment ratio increased with the decrease of rock plate Young's modulus. When the rock plate had the same Young's modulus, compared to fractures filled with mesh-20/40 particles, proppant embedment ratios were smaller for fractures filled with mesh-40/70 particles, homogenous particles, and two layers of particles. This was because, under these three scenarios, more particles were in direct contact with the rock surface, leading to lower load on individual particles and thereby smaller proppant embedment ratios. Fig. 23b demonstrates fracture conductivities as a function of closure pressure. The simulation results clearly demonstrated that rock plates with a

higher Young's modulus had higher fracture conductivities for all scenarios. When the effective stress increases to 41.4 MPa, the fracture conductivity decreased significantly, because most particles were crushed and the generated fine-sized particles can block the flow channels, leading to lower fracture conductivities. It was also observed that the fracture conductivity increased with the number of proppant layers. Compared with the fractures supported by mesh-20/40 particles, fractures supported by mesh-40/70 particles were less sensitive to the variations in Young's moduli of the rock plates. When the rock plate had a relatively high Young's modulus (e.g., 20 GPa), the proppant diameter distribution played a less important role on the fracture conductivity.

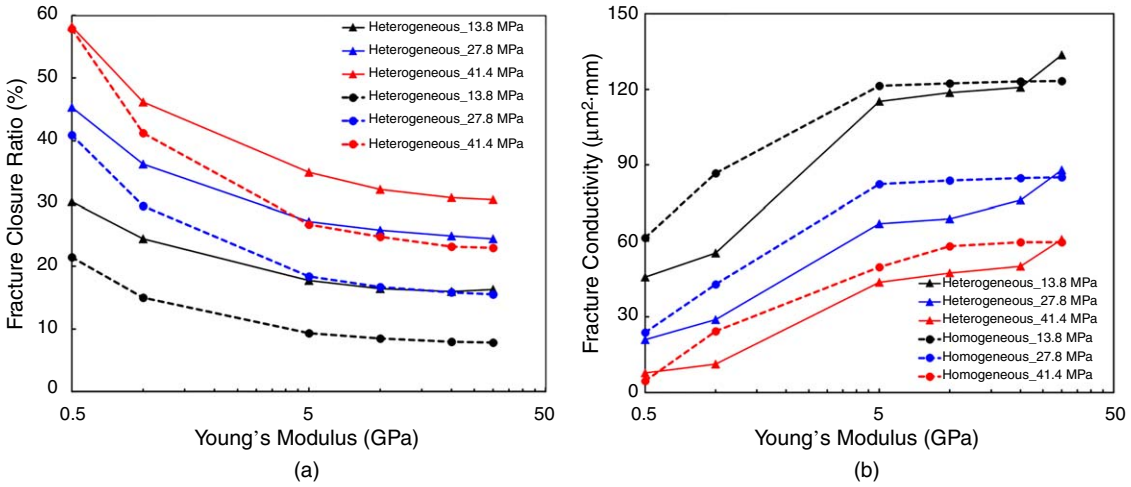

Fig. 21—(a) Fracture width reduction and (b) fracture conductivity as a function of rock plate Young's modulus for fractures supported by monolayers of proppants with homogeneous and heterogeneous particle-diameter distributions.

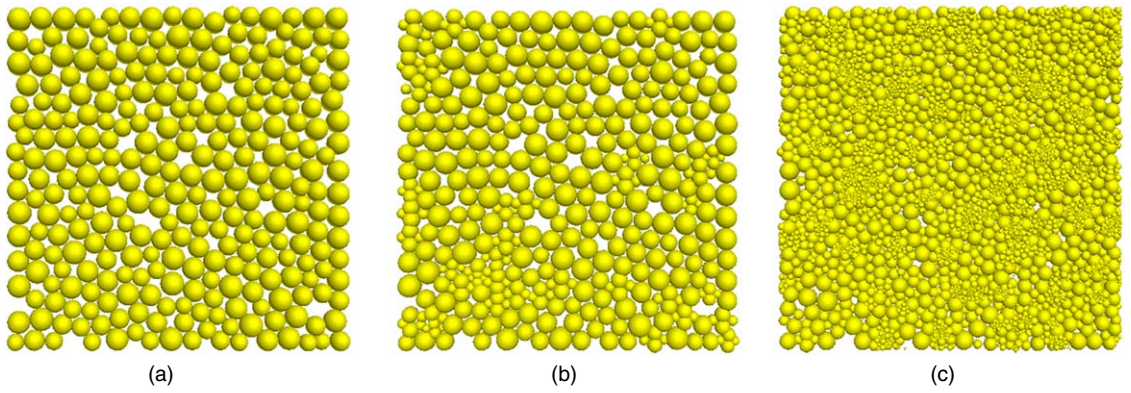

Fig. 22—Proppant pack of sand particles under closure pressures of (a) 13.8 MPa, (b) 27.8 MPa, and (3) 41.4 MPa. The development of fine-sized particles was due to proppant crushing under increasing closure pressures. The fracture was filled with a monolayer of sand particles between two sandstone rock plates having a Young's modulus of 20 GPa.

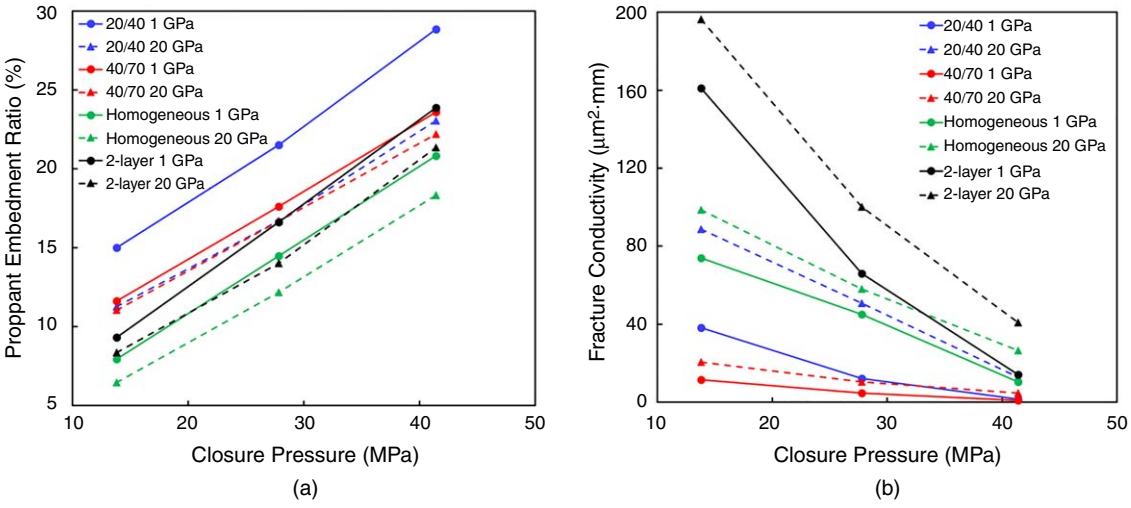

Fig. 23—(a) Proppant embedment ratio and (b) fracture conductivity as a function of closure pressure. "1 GPa" and "20 GPa" represent the rock plate Young's modulus; "20/40" and "40/70" represent the proppant particle size; "homogeneous" indicates a monolayer of homogeneous proppant particles with a particle diameter of 0.63 mm; and "2-layer" indicates two layers of sand particles having a size distribution of mesh-size 20/40.

Conclusions

In this work, a comprehensive experimental and numerical study was conducted to evaluate the factors affecting proppant embedment in narrow fractures. Through fracture conductivity experiments, the influence of rock/fluid interaction, fracture surface roughness, and proppant type on the changes in proppant embedment was investigated. A coupled numerical workflow combing FLAC3D/PFC3D with LB simulator was then developed to evaluate the role of proppant layer number, proppant size, proppant diameter distribution, and proppant particle crushing on the changes in fracture width and conductivity when rock plates have various Young's moduli. The simulated fracture/proppant system can demonstrate more realistic interactions between proppants, hydraulic fractures, and closure pressure. Moreover, the proposed numerical workflow provides a more efficient and economical way for proppant parameter selections without carrying out time-consuming fracture-conductivity experiments. Based on the experimental and numerical studies, the following conclusions can be drawn:

1. Fractures supported by monolayers of sand particles cannot maintain sufficient fracture conductivities even when proppant embedment is mitigated in softened rock formations due to the interaction between the rock plate and fracturing fluid. Compared with the short-term interaction, the long-term rock/fluid interaction can result in significant proppant embedment and severe damage to the fracture conductivity in monolayer-propped fractures.
2. In a monolayer-propped fracture, the fracture having a rough rock surface has higher fracture width and conductivity because of the alleviated proppant embedment and increased fracture permeability.
3. There is a strong relationship between rock mechanical properties and proppant embedment. When the Young's modulus of the rock plate exceeds 5 GPa, ceramic proppant embedment can be alleviated considerably.
4. When the rock plate is softened significantly due to the rock/fluid interaction, mechanical support from two or more layer numbers of proppant can help to minimize the effect of proppant embedment and to maintain the conductivity in narrow fractures.
5. The proppant size study demonstrates that proppant particles having large diameters are more sensitive to the changes of Young's modulus of the rock plate. For narrow fractures supported by small mesh-size proppants (e.g., 40/70 or 100), the long-term fracture conductivity can be maintained more easily because fractures can be supported by more proppant particles.
6. When the rock formation has a relatively high Young's modulus, the proppant particle-diameter distribution has a lesser effect on the fracture conductivity in narrow-fracture environments.

Nomenclature

$\boldsymbol{e}_i$ = lattice velocity vector, m/s
E_a = apparent modulus, GPa
f_i = particle-distribution function
$F_j^{(c)}$ = jth component of the force magnitude of contact c, N
$\boldsymbol{k}$ = permeability tensor, m^2
k^n = normal stiffness at the contact, N/m
k^S = shear stiffness at the contact, N/m
kwf = conductivity of the propped fracture, $\mu m^2 \cdot cm$
L = distance between pressure ports, cm
n_c = number of contacts
$n_i^{(c)}$ = ith component of the unit direction vector of contact c, dimensionless
Q = flow rate, cm^3/s
R_a = mean peak-to-valley height, mm
R_p = mean peak height, mm
R_v = mean valley depth, mm
t = time, seconds
$\mathbf{v}$ = Darcy velocity, m/s
W = width of the conductivity cell, cm
x = location, m
Δp = pressure drop, kPa
Δt = timestep, seconds
Δx = lattice spacing, m
μ = dynamic viscosity, mPa·s
ρ = density, kg/m^3
τ = relaxation time, dimensionless
ω_i = weights for D3Q19 model

Author Contributions

Ming Fan: conceptualization, methodology, software, model construction and validation, result analysis, writing original draft and editing. **Zihao Li**: methodology and result analysis. **Yanhui Han**: methodology, software, model construction, result analysis, writing-review, and editing. **Yuntian Teng**: methodology and result analysis. **Cheng Chen**: conceptualization, methodology, result analysis, supervision, writing-review, and editing.

Declaration of Interests

We declare that we have no known competing financial interest or personal relationships that could have appeared to influence the work reported in this paper.

Acknowledgments

We acknowledge the funding support from the American Chemical Society Petroleum Research Fund (ACS-PRF) under the award number of 60105-ND9. We are also thankful to the support from Aramco Research Center–Houston.

References

Alramahi, B. and Sundberg, M. I. 2012. Proppant Embedment and Conductivity of Hydraulic Fractures in Shales. Paper presented at the 46th US Rock Mechanics/Geomechanics Symposium, Chicago, Illinois, USA, 24–27 June. ARMA-2012-291.

API RP-19D, *Measuring the Long-Term Conductivity of Proppants*. 2008. Washington, DC, USA: API.

Bandara, K. M. A. S., Ranjith, P. G., and Rathnaweera, T. D. 2019. Improved Understanding of Proppant Embedment Behavior under Reservoir Conditions: A Review Study. *Powder Technol* **352**: 170–192. https://doi.org/10.1016/j.powtec.2019.04.033.

Chen, C., Hu, D., Westacott, D. et al. 2013. Nanometer-Scale Characterization of Microscopic Pores in Shale Kerogen by Image Analysis and Pore-Scale Modeling. *Geochem Geophys Geosyst* **14** (10): 4066–4075. https://doi.org/10.1002/ggge.20254.

Chen, C., Lau, B. L. T., Gaillard, J.-F. et al. 2009a. Temporal Evolution of Pore Geometry, Fluid Flow, and Solute Transport Resulting from Colloid Deposition. *Water Resour Res* **45** (6): W06416. https://doi.org/10.1029/2008WR007252.

Chen, C., Martysevich, V., O'Connell, P. et al. 2015. Temporal Evolution of the Geometrical and Transport Properties of a Fracture/Proppant System under Increasing Effective Stress. *SPE J*. **20** (3): 527–535. SPE-171572-PA. https://doi.org/10.2118/171572-PA.

Chen, C., Packman, A. I., and Gaillard, J.-F. 2008. Pore-Scale Analysis of Permeability Reduction Resulting from Colloid Deposition. *Geophys Res Lett* **35** (7): L07404. https://doi.org/10.1029/2007GL033077.

Chen, C., Packman, A. I., and Gaillard, J.-F. 2009b. Using X-Ray Micro-Tomography and Pore-Scale Modeling To Quantify Sediment Mixing and Fluid Flow in a Developing Streambed. *Geophys Res Lett* **36** (8): L08403. https://doi.org/10.1029/2009GL037157.

Chen, C., Wang, Z., Majeti, D. et al. 2016. Optimization of Lattice Boltzmann Simulation with Graphics-Processing-Unit Parallel Computing and the Application in Reservoir Characterization. *SPE J*. **21** (4): 1425–1435. SPE-179733-PA. https://doi.org/10.2118/179733-PA.

Chen, S. and Doolen, G. D. 1998. Lattice Boltzmann Method for Fluid Flows. *Annu Rev Fluid Mech* **30**: 329–364. https://doi.org/10.1146/annurev.fluid.30.1.329.

Cui, A., Glover, K., and Wust, R. A. J. 2014. Elastic and Plastic Mechanical Properties of Liquids-Rich Unconventional Shales and Their Implications for Hydraulic Fracturing and Proppant Embedment: A Case Study of the Nordegg Member in Alberta, Canada. Paper presented at the 48th US Rock Mechanics/Geomechanics Symposium, Minneapolis, Minnesota, USA, 1–4 June. ARMA-2014-7556.

Cundall, P. A. 1971. A Computer Model for Simulating Progressive Large-Scale Movements in Blocky Rock Systems. In *Rock Fracture: Proceedings of the International Symposium on Rock Mechanics*, Nancy, France, 4–6 October, Vol. 2, 2–8. International Society for Rock Mechanics.

Cundall, P. A. and Strack, O. D. 1979. A Discrete Numerical Model for Granular Assemblies. *Géotechnique* **29** (1): 47–65. https://doi.org/10.1680/geot.1979.29.1.47.

Darin, S. R. and Huitt, J. L. 1960. Effect of a Partial Monolayer of Propping Agent on Fracture Flow Capacity. In *Transactions of the Society of Petroleum Engineers*, Vol. 219, Part 1, SPE-1291-G, 31–37. Richardson, Texas, USA: Society of Petroleum Engineers. https://doi.org/10.2118/1291-G.

Fan, M. and Chen, C. 2020. Numerical Simulation of the Migration and Deposition of Fine Particles in a Proppant-Supported Fracture. *J Pet Sci Eng* **194**: 107484. https://doi.org/10.1016/j.petrol.2020.107484.

Fan, M., Han, Y., Gu, M. et al. 2019a. Combining Discrete Element Method with Lattice Boltzmann Modeling To Advance the Understanding of the Performance of Proppant Mixtures. Paper presented at the 53rd US Rock Mechanics/Geomechanics Symposium, New York, New York, USA, 23–26 June. ARMA-2019-1668.

Fan, M., Han, Y., Gu, M. et al. 2020. Investigation of the Conductivity of a Proppant Mixture Using an Experiment/Simulation-Integrated Approach. *J Nat Gas Sci Eng* **78**: 103234. https://doi.org/10.1016/j.jngse.2020.103234.

Fan, M., Han, Y., and McClure, J. 2017a. Hydraulic Fracture Conductivity as a Function of Proppant Concentration under Various Effective Stresses: From Partial Monolayer To Multilayer Proppants. Paper presented at the SPE/AAPG/SEG Unconventional Resources Technology Conference, Austin, Texas, USA, 24–26 July. URTEC-2017-2693347-MS. https://doi.org/10.15530/URTEC-2017-2693347.

Fan, M., Han, Y., McClure, J. et al. 2018a. Investigating the Impact of Proppant Embedment and Compaction on Fracture Conductivity Using a Continuum Mechanics, DEM, and LBM Coupled Approach. Paper presented at the 52nd U.S. Rock Mechanics/Geomechanics Symposium, Seattle, Washington, USA, 17–20 June. ARMA-2018-357.

Fan, M., McClure, J., Han, Y. et al. 2017b. Interaction between Proppant Packing, Reservoir Depletion, and Fluid Flow in Hydraulic Fractures. Paper presented at the Offshore Technology Conference, Houston, Texas, USA, 1–4 May. OTC-27907-MS. https://doi.org/10.4043/27907-MS.

Fan, M., McClure, J., Han, Y. et al. 2018b. Interaction between Proppant Compaction and Single-/Multiphase Flows in a Hydraulic Fracture. *SPE J*. **23** (4): 1290–1303. SPE-189985-PA. https://doi.org/10.2118/189985-PA.

Fan, M., McClure, J., Han, Y. et al. 2019b. Using an Experiment/Simulation Integrated Approach To Investigate Fracture-Conductivity Evolution and Non-Darcy Flow in a Proppant-Supported Hydraulic Fracture. *SPE J*. **24** (4): 1912–1928. SPE-195588-PA. https://doi.org/10.2118/195588-PA.

Fuss, T., Shi, J., Bottiglieri, S. et al. 2016. Evaluation of Sand and Ceramic Proppant Performance Under Thin Layer/Monolayer Conditions of Unconventional Hydraulic Fractures. Paper presented at the SPE Low Perm Symposium, Denver, Colorado, USA, 5–7 May. SPE-180261-MS. https://doi.org/10.2118/180261-MS.

Gu, M., Fan, M., and Chen, C. 2017. Proppant Optimization for Foam Fracturing in Shale and Tight Reservoirs. Paper presented at the SPE Unconventional Resources Conference, Calgary, Alberta, Canada, 15–16 February. SPE-185071-MS. https://doi.org/10.2118/185071-MS.

Guo, J. and Liu, Y. 2012. Modeling of Proppant Embedment: Elastic Deformation and Creep Deformation. Paper presented at the SPE International Production and Operations Conference and Exhibition, Doha, Qatar, 14–16 May. SPE-157449-MS. https://doi.org/10.2118/157449-MS.

Herskovits, R., Kidd, I., Fuss-Dezelic, T. et al. 2017. Mono & Thin Layer Performance of Small Mesh Size Proppants Placed in Horizontal Well Fracture Matrices. Paper presented at the SPE Annual Technical Conference and Exhibition, San Antonio, Texas, USA, 9–11 October. SPE-187449-MS. https://doi.org/10.2118/187449-MS.

Inamuro, T., Yoshino, M., and Ogino, F. 1999. Lattice Boltzmann Simulation of Flows in a Three-Dimensional Porous Structure. *Int J Numer Methods Fluids* **29** (7): 737–748. https://doi.org/10.1002/(SICI)1097-0363(19990415)29:7%3C737::AID-FLD813%3E3.0.CO;2-H.

Itasca Consulting Group. 2008. *PFC3D—Particle Flow Code in 3 Dimensions, Version 4.0 User's Manual*. Minneapolis, Minnesota, USA: Itasca Consulting Group.

Itasca Consulting Group. 2012. *FLAC3D, Fast Lagrangian Analysis of Continua in 3 Dimensions, Version 5.0*. Minneapolis, Minnesota, USA: Itasca Consulting Group.

Jansen, T. A., Zhu, D., and Hill, A. D. 2015. The Effect of Rock Mechanical Properties on Fracture Conductivity for Shale Formations. Paper presented at the SPE Hydraulic Fracturing Technology Conference, The Woodlands, Texas, USA, 3–5 February. SPE-173347-MS. https://doi.org/10.2118/173347-MS.

Karatza, Z., Andò, E., Papanicolopulos, S. A. et al. 2019. Effect of Particle Morphology and Contacts on Particle Breakage in a Granular Assembly Studied Using X-Ray Tomography. *Granular Matter* **21** (3): 44. https://doi.org/10.1007/s10035-019-0898-2.

Khanna, A., Kotousov, A., Sobey, J. et al. 2012. Conductivity of Narrow Fractures Filled with a Proppant Monolayer. *J Pet Sci Eng* **100**: 9–13. https://doi.org/10.1016/j.petrol.2012.11.016.

Li, Z., Ripepi, N., and Chen, C. 2019. Comprehensive Laboratory Investigation and Model Fitting of Klinkenberg Effect and Its Role on Apparent Permeability in Various US Shale Formations. Paper presented at the 53rd U.S. Rock Mechanics/Geomechanics Symposium, New York, New York, USA, 23–26 June. ARMA-2019-1568.

Li, Z., Ripepi, N., and Chen, C. 2020. Using Pressure Pulse Decay Experiments and a Novel Multi-Physics Shale Transport Model To Study the Role of Klinkenberg Effect and Effective Stress on the Apparent Permeability of Shales. *J Pet Sci Eng* **189**: 107010. https://doi.org/10.1016/j.petrol.2020.107010.

Liang, F., Han, Y., Liu, H. H. et al. 2020. An Improved Hydraulic Fracturing Treatment for Stimulating Tight Organic-Rich Carbonate Reservoirs. *SPE J*. **25** (2): 632–645. SPE-199880-PA. https://doi.org/10.2118/199880-PA.

Liang, F., Sayed, M., Al-Muntasheri, G. A. et al. 2016. A Comprehensive Review on Proppant Technologies. *Petroleum* **2** (1): 26–39. https://doi.org/10.1016/j.petlm.2015.11.001.

Nakata, Y., Kato, Y., Hyodo, M. et al. 2001. One-Dimensional Compression Behaviour of Uniformly Graded Sand Related to Single Particle Crushing Strength. *Soils Found* **41** (2): 39–51. https://doi.org/10.3208/sandf.41.2_39.

Perez Pena, P., Zhu, D., and Hill, A. D. 2016. The Effect of Rock Properties on Fracture Conductivity in the Marcellus Shale. Paper presented at the SPE Asia Pacific Hydraulic Fracturing Conference, Beijing, China, 24–26 August. SPE-181867-MS. https://doi.org/10.2118/181867-MS.

Potyondy, D. O. and Cundall, P. A. 2004. A Bonded-Particle Model for Rock. *Int J Rock Mech Min Sci* **41** (8): 1329–1364. https://doi.org/10.1016/j.ijrmms.2004.09.011.

Santos, P. M. D. and Júlio, E. N. B. S. 2013. A State-of-the-Art Review on Roughness Quantification Methods for Concrete Surfaces. *Constr Build Mater* **38**: 912–923. https://doi.org/10.1016/j.conbuildmat.2012.09.045.

Singh, V. K., Wolfe, C., and Jiao, D. 2019. Fracturing Fluids Impact on Unconventional Shale Rock Mechanical Properties and Proppant Embedment. Paper presented at the 53rd U.S. Rock Mechanics/Geomechanics Symposium, New York, New York, USA, 23–26 June. ARMA-2019-1831.

Stegent, N. A., Wagner, A. L., Mullen, J. et al. 2010. Engineering a Successful Fracture-Stimulation Treatment in the Eagle Ford Shale. Paper presented at the Tight Gas Completions Conference, San Antonio, Texas, USA, 2–3 November. SPE-136183-MS. https://doi.org/10.2118/136183-MS.

Succi, S. 2001. *The Lattice Boltzmann Equation: For Fluid Dynamics and Beyond*. Oxford, England, UK: Oxford University Press.

Tang, Y., Ranjinth, P. G., Perera, M. S. A. et al. 2018. Influences of Proppant Concentration and Fracturing Fluids on Proppant-Embedment Behavior for Inhomogeneous Rock Medium: An Experimental and Numerical Study. *SPE Prod & Oper* **33** (4): 666–678. SPE-189984-PA. https://doi.org/10.2118/189984-PA.

Wang, T., Huang, H., Zhang, F. et al. 2020. DEM-Continuum Mechanics Coupled Modeling of Slot-Shaped Breakout in High-Porosity Sandstone. *Tunnelling Underground Space Technol* **98**: 103348. https://doi.org/10.1016/j.tust.2020.103348.

Zhang, F., Zhu, H., Zhou, H. et al. 2017. Discrete-Element-Method/Computational-Fluid-Dynamics Coupling Simulation of Proppant Embedment and Fracture Conductivity after Hydraulic Fracturing. *SPE J*. **22** (2): 632–644. SPE-185172-PA. https://doi.org/10.2118/185172-PA.

Zhang, J., Ouyang, L., Zhu, D. et al. 2015. Experimental and Numerical Studies of Reduced Fracture Conductivity due to Proppant Embedment in the Shale Reservoir. *J Pet Sci Eng* **130**: 37–45. https://doi.org/10.1016/j.petrol.2015.04.004.

Zheng, W., Silva, S. C., and Tannant, D. D. 2018. Crushing Characteristics of Four Different Proppants and Implications for Fracture Conductivity. *J Nat Gas Sci Eng* **53**: 125–138. https://doi.org/10.1016/j.jngse.2018.02.028.

Zheng, W. and Tannant, D. D. 2019. Influence of Proppant Fragmentation on Fracture Conductivity—Insights from Three-Dimensional Discrete Element Modeling. *J Pet Sci Eng* **177**: 1010–1023. https://doi.org/10.1016/j.petrol.2019.03.015.

Zhong, Y., Kuru, E., Zhang, H. et al. 2019. Effect of Fracturing Fluid/Shale Rock Interaction on the Rock Physical and Mechanical Properties, the Proppant Embedment Depth and the Fracture Conductivity. *Rock Mech Rock Eng* **52** (4): 1011–1022. https://doi.org/10.1007/s00603-018-1658-z.

Zhu, H., Shen, J., and Zhang, F. 2019. A Fracture Conductivity Model for Channel Fracturing and Its Implementation with Discrete Element Method. *J Pet Sci Eng* **172**: 149–161. https://doi.org/10.1016/j.petrol.2018.09.054.